CALIFORNIA INSTITUTE OF TECHNOLOGY

BIG BEAR SOLAR OBSERVATORY

HALE OBSERVATORIES

THICK TARGET MODELS OF IMPULSIVE CHROMOSPHERIC FLARES

Barry J. LaBonte

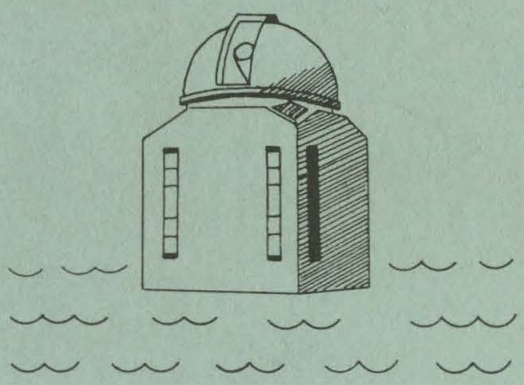

THICK TARGET MODELS
OF
IMPULSIVE CHROMOSPHERIC FLARES

Barry J. LaBonte

Big Bear Solar Observatory, Hale Observatories
Carnegie Institution of Washington
California Institute of Technology
Pasadena, California 91125

BBSO #0173
June, 1978

ABSTRACT

The most impulsive flares show large amplitude intensity variations in times of order 10 s. An attempt is made to reproduce the properties of these events with a model in which the heating of a static chromosphere by a nonthermal electron beam is balanced by thermal radiation cooling. The computed results suggest that the assumed static equilibrium may be achieved in some parts of the flares, and indicate improvements necessary for more accurate models of this type of flare.

1. INTRODUCTION

Risetimes of solar flares vary from seconds (Zirin, 1977) to hours (Sheeley et al., 1975; Kahler, 1977). The intensities of the chromospheric flare phenomena appear to be inverse to the risetime. Flares with the most rapid evolution, those with prominent chromospheric impulsive phases, are of particular interest.

Observationally, impulsive flares produce the largest optical emission intensities and linewidths (Zirin and Tanaka, 1973). These reflect high electron densities, and the alteration of the chromosphere at great depths. Microwave, meterwave, and hard X-ray emissions indicate the presence of energetic nonthermal electron beams, and important nonequilibrium processes. In some flares, this nonthermal process may release an energy comparable to the total flare energy (Lin and Hudson, 1976).

In many models of flare plasma mechanisms, the impulsive phase occurs just as the flare is "triggered", the moment at which the quiescent plasma processes fail to relax the increasing stresses (Sturrock, 1968; Heyvaerts et al., 1977). The onset of plasma instabilities allows the dissipation of the stored energy in the flare. Study of the impulsive phenomena may reveal the nature of the flare instability, since the fastest evolving phenomena have presumably been least altered by propagation effects between

the flare instability and the observer.

Finally, the extreme-ultraviolet radiation flash from the impulsive flare produces the strongest unpredictable terrestrial effect, the sudden ionospheric disturbance (Donnelly, 1971). Other flare phenomena with terrestrial impact, such as particle fluxes or shock waves, propagate slower than the velocity of light, and can be anticipated once the flare is observed optically.

We report here on an attempt to model the properties of the chromosphere in one type of impulsive flare. The prominent characteristic of these events is rapid optical emission flashing in high excitation lines. Knots 1 to 5 arcseconds in extent exhibit 100% intensity modulation on 5 to 10 second time scales. These events have been observed in high Balmer lines (Zirin and Tanaka, 1973) and He I D_3 (LaBonte, 1978). In the one case where data are available, the optical emission is simultaneous with nonthermal hard X-ray emission, which also has large amplitude intensity modulation on few second time scales (Van Beek et al., 1973).

The simultaneity of nonthermal hard X-rays with the impulsive phase of optical flares is well established in the general phase (Vorpahl, 1972; Zirin, 1973). Correlated, rapid, low amplitude intensity fluctuations in X-rays and optical continuum emission have also been observed (Rust and Hegwer, 1975). The type of event we describe thus represents

the extreme, in terms of intensity modulation on short time scales, of flares with related optical and nonthermal X-ray emission.

As with most impulsive events, these flashes are not the entirety of the optical flare, but only one phase. However, an individual flare may have several impulsive knots, which in part accounts for events with long-lived nonthermal X-ray emission. A second type of long-lived nonthermal event to which our models may also apply is the case of a steady energy flux, with variation only in the position on the chromosphere which is bombarded. A point would be heated only briefly compared with the total duration of the X-ray emission. This type of event produces a "wave" of optical emission (Zirin and Tanaka, 1973; Machado and Rust, 1974).

The interpretation we apply to these events has been suggested for the general case (Hudson, 1972; Syrovatskii and Shmeleva, 1972). A beam of nonthermal electrons, accelerated in the corona, moves downward, impacting and heating the chromosphere. X-ray emission is produced by thick target bremsstrahlung, optical emission by thermal radiation. The rapid intensity modulation of the emitted radiation is a response to variation in the electron beam flux.

The model calculations begin with a one-dimensional,

hydrostatic quiet chromosphere. It is assumed that in the flare a steady state atomic equilibrium is reached, with the electron heating in each volume balanced by thermal radiative cooling, thus determining the temperature and ionization structure. The density distribution is assumed not to relax in response to the increased temperatures in the brief duration of the flare.

Three topics are of interest. First, it must be determined whether the flare chromosphere can in fact reach a radiative equilibrium state (yet hydrodynamic effects be ignored), or if time dependent calculations are required. Second, if such an equilibrium can be achieved, it is necessary to see whether the models predict observed X-ray and optical emission intensities. Lin and Hudson (1976) and Zirin (1977) have suggested that nonthermal processes are important contributors to optical emissions. Third, the actual model results must be displayed for comparison with time dependent or nonthermal calculations. The equilibrium case may be a useful approximation, even if not strictly valid. Because the models must be calculated numerically, these points will be addressed in inverted order.

Note that Brown (1973) has computed thick target flare models; however, Lin and Hudson (1976) and Canfield (1974a) have pointed out errors in the heating and cooling equations used. In addition, Brown considered longlived flares,

allowing the density distribution to relax to the flare temperatures, a process unlikely to be important in short-lived flashes (Bessey and Kuperus, 1970).

2. MODEL PHYSICS

In this section, the physical basis of the models is described.

2.1 Preflare Atmospheric Structure

The model of Vernazza et al. (1973) is used to represent the preflare chromosphere. While the chromosphere is actually inhomogeneous at high altitude, the densities in structures such as spicules and prominences are $\lesssim 10^{11}$ cm^{-3} (Beckers, 1972; Heasley et al., 1974); to produce emission in the high excitation lines observed in the flashes requires higher densities, $\gtrsim 10^{12}$ cm^{-3} (e.g., Kulander, 1976). At the lower altitudes corresponding to the higher densities, a one dimensional, hydrostatic model may be a reasonable approximation.

Any magnetic field present is assumed to be constant with height and vertical. The electron beam is directed vertically downward, with the integral density (cm^{-2}) traversed by the beam at any height just the vertical integral of the volume density, $N(H) = \int_H^\infty n(h)\,dh$ Since the structure of the magnetic field is not well determined at the heights of interest, this is a useful approximation. Increasing field strength with depth (field line convergence) would concentrate and/or mirror the beam particles; nonvertical direction would increase N(H).

The quiet chromosphere's elevated temperature is maintained by some form of energy input, presumably a form of wave dissipation. We assume this heating is not increased in the flare. The nonflare heating per unit volume, G_Q, is taken to be equal to the radiative cooling calculated for the quiet atmosphere by the same methods used for the flares (Section 2.3). This nonflare term must be included in order to retrieve the quiet model temperature at depths in the flares for which electron heating is small.

Height is measured upward from the level $\tau_{5000\ \mathring{A}} = 1$ in the photosphere. The lower boundary for the flare models is 500 km, the height of the quiet temperature minimum. The top of the quiet model (the transition zone height) is 2400 km. We assume the mass above that height is zero, which is effectively true for the electron energies of interest.

2.2 Nonthermal Electron Heating

Hard X-ray (photon energies $\gtrsim$ 10 keV) flare spectra are very nearly power laws, $f(h\nu) = A(h\nu)^{-\gamma}$ photons-(cm^2-s-keV)$^{-1}$, with $h\nu$ the photon energy in keV. Most flares have spectral indices in the range $3 \lesssim \gamma \lesssim 5$; at Earth, peak values of f(20) range from the threshold of $\simeq$ 0.1 up to $\simeq$ 400, with the number of flares having $f(20) \geq f_o$ proportional to f_o^{-1} (Datlowe, 1974; Lin and Hudson, 1976).

The nonthermal spectrum is usually characterized at 20 keV as it is clearly evident at that energy. At low energies, it is covered by thermal emission from the 10^7 K (1 keV) coronal flare plasma. In a few favorable cases, the power law has been observed down to 3 to 5 keV (Kahler and Kreplin, 1971; Peterson et al., 1973). In no case has the power law been reported to flatten at an energy above the thermal emission, although it must turn over at some low energy. At high energies, $\simeq$ 100 keV, the power law is often observed to steepen, with an increase in spectral index of order 0.5 to 2 (Kane and Anderson, 1970; Frost and Dennis, 1971; Van Beek et al., 1973).

To relate the X-ray spectrum to the electron beam heating, we use the formulae of Lin and Hudson (1976). The X-ray spectrum can be inverted in the thick target case to determine the differential electron beam spectrum,

$$\frac{dn_e}{d\varepsilon} \propto \varepsilon^{-\gamma-1} \quad \text{electrons-keV}^{-1}\text{-s}^{-1},$$

ε the electron energy in keV. This in turn can be integrated to give the total energy in nonthermal electrons,

$$E_t(\varepsilon_L) = \int_{\varepsilon_L}^{\infty} \frac{dn_e}{d\varepsilon}\, \varepsilon\, d\varepsilon = 9.4 \times 10^{24}\, b(\gamma)\, A \frac{\varepsilon_L^{-\gamma+1}}{\gamma-1} \text{ ergs-s}^{-1}, \tag{1}$$

with $b(\gamma) = \gamma^2(\gamma-1)^2\, \beta(\gamma-\frac{1}{2},\frac{3}{2}) \simeq 2(\gamma-1)^2$, and β the complete beta function. The lower limit on the integration, ε_L, is

necessary to keep the total energy finite. Generally, one uses ε_L = 20 keV.

The total nonthermal energy is an integral of the nonthermal flux over the flare area,

$$E_{20} = \int_{\text{flare}} F_{20}\, da\ . \tag{2}$$

There are no spatially resolved hard X-ray observations to show the partitioning of the nonthermal flux, but distributing observed nonthermal energies over flare areas, the typical range of F_{20} is found to be $10^8 \lesssim F_{20} \lesssim 10^{11}$ ergs-cm^{-2}-s^{-1}. Our models are one dimensional and can be parameterized by the flux F_{20}. We will compute a grid of twelve models, with $F_{20} = 10^8, 10^9, 10^{10}, 10^{11}$ ergs-cm^{-2}-s^{-1}, and γ = 3, 4, 5.

Energy deposition by the electron beam falls off with depth in the atmosphere. The energy gained by a volume at integral density N(cm^{-2}) is,

$$G_F(N) = 1.1 \times 10^{18}\, (\gamma-1)\, 20^{\gamma-1}\, F_{20}\, \beta(\tfrac{\gamma+1}{2},\tfrac{1}{3}) \times$$

$$(1.1 \times 10^{-17} N)^{-(\frac{\gamma+1}{2})}\, [X(N) + 0.55]\, n(N) \text{ ergs-cm}^{-3}\text{-s}^{-1}, \tag{3}$$

with X the fractional ionization, n the total particle (ions plus neutrals) volume density. The quantity

$$\varepsilon_N = (1.1 \times 10^{-17}\, N)^{\frac{1}{2}} \text{ keV} \tag{4}$$

is often referred to as the electron energy whose range is N.

Equation 3 does not assume a low energy cutoff in the electron spectrum. If such a cutoff exists, with $\frac{dn_e}{d\mathcal{E}} = 0$ for $\mathcal{E} < \mathcal{E}_C$, the equation remains valid for $\mathcal{E}_N > \mathcal{E}_C$, but, for $\mathcal{E}_N < \mathcal{E}_C$, the complete beta function $\beta(\frac{\gamma+1}{2}, \frac{1}{3})$ is replaced by the incomplete beta function, $\beta_z(\frac{\gamma+1}{2}, \frac{1}{3})$, $z = (\mathcal{E}_N/\mathcal{E}_C)^2$. We will use equation 3 as written. The lack of observations weighs against including an arbitrary low energy cutoff to the power law spectrum. In fact, other considerations will determine a lowest energy which contributes to the part of the flare in radiative equilibrium (Section 2.3.3). Inclusion of a high energy steepening will not turn out to be important (Section 4.1).

Instability of the electron beam is not considered; the most important problem, the need for a return current, apparently is resolved in a few seconds without major disruption of the beam (Knight and Sturrock, 1977).

2.3 Thermal Radiative Cooling

The thermal radiative cooling of a plasma has been tabulated by Cox and Tucker (1969) for the case in which the atmosphere is optically thin at all wavelengths. Unfortunately, the flare chromosphere is optically thick in many important transitions. This is obvious for

resonance transitions of abundant species (H, He, C, O, etc.) as well as subordinate lines which are deep in the quiet chromosphere (Balmer series); in dense parts of the flare, even higher ionization stages will be numerous enough to have deep lines. The computation of several transitions for each of the important species would be complex and probably not justified given the simplicity in handling other physical processes. Our solution will be to compute the hydrogen system explicitly, as it should be a major contributor to cooling, its ionization sets the electron density for the whole flare, and its emissions are observed in the optical flashes. Cooling from metals will be included by correcting the optically thin values in a way consistent with the effects of optical depth.

2.3.1 Hydrogen

Lyman α and Hα are assumed to dominate the cooling from atomic hydrogen (Canfield, 1974a) and are the only transitions included in the model. The model hydrogen atom thus has three bound levels. Since other transitions are ignored, these lines are computed in the two level approximation, with the excitation described by the source function S,

$$S = \frac{J + \epsilon B}{1 + \epsilon} , \qquad (5)$$

where J is the frequency averaged mean intensity, B the

Planck function, and $\epsilon = C_{UL}/A_{UL}$, the ratio of collisional to radiative deexcitation rates.

Line emission cools a volume by the amount

$$dQ = n_U A_{UL} h\nu \rho \tag{6}$$

with n_U the upper level number density, $h\nu$ the photon energy, and

$$\rho = 1 - \frac{J}{S} = \epsilon \left(\frac{B}{S} - 1\right) \tag{7}$$

is the net radiative bracket (Canfield, 1974b). In an optically thin line, no intensity is built up by scattering, and $\rho = 1$; in a deep line, $\rho \ll 1$ as most of the emitted photons are promptly reabsorbed and do not decrease the energy of the gas.

The ionization is set by radiative and collisional processes in the optically thin Balmer and Paschen continua, plus collisions in the Lyman continuum, which is assumed in radiative detailed balance. Bound level population ratios are set by the lines,

$$\frac{n_U}{n_L} = \frac{g_U}{g_L}\left[\frac{2h\nu^3}{c^2}\,\frac{1}{S} + 1\right]^{-1}, \tag{8}$$

with g the statistical weight, c the speed of light. The sum of all bound and free densities equals the total hydrogen density, n_H.

The problem with an optically thick line is the

calculation of J, which depends on the emission and absorption (thus, n_U, n_L) throughout the atmosphere. We use the probabilistic method (Athay, 1972a), with many of the details from Canfield (1974a, b). [Note that there are several errors in the programs of Canfield (1974c); when corrected, the probabilistic method is more accurate than Canfield (1974b) shows.] P_c, P_d, P_e are, respectively, the probabilities per scattering that a photon is created, destroyed, or escapes from the atmosphere. The mean number of scatterings before escape is $N_s = P_e^{-1}$. From Athay,

$$P_c = P_d\, B/J\ ; \tag{9a}$$

$$P_d = \frac{\epsilon}{1+\epsilon}\ ; \tag{9b}$$

$$P_e = \frac{1}{2 + \tau[\pi \ln(\tau + e)]^{\frac{1}{2}}} + \frac{a}{2 + \pi^{\frac{3}{4}}\,\tau^{\frac{1}{2}}}\ ; \tag{9c}$$

where τ is the line center optical depth and a the ratio of damping to Doppler linewidths. Doppler broadening by thermal and preflare turbulent velocities is included in computing the optical depth. Then,

$$J(N_s) = J(N_T) - (2N_s)^{\frac{1}{2}} \exp(t_s^2) \int_{t_s}^{t_T} P_d^{\frac{1}{2}}\, B \exp(-t_j^2)\, dt_j \tag{10}$$

with $t_k = (P_d N_k/2)^{\frac{1}{2}}$. For a boundary condition we use $J(N_T) = B(N_T)$, where N_T is effectively a thermalization

depth, defined by $P_d(N_T) = P_e(N_T)$. These equations assume noncoherent scattering.

The densities (which determine the probabilities) and radiation fields are computed alternately until a consistent solution is obtained. The cooling is then calculated. From each finished model the actual observable emission is also computed,

$$E = \int n_U A_{UL} h\nu P_e \, dh. \qquad (11)$$

It is expected that $E \simeq Q$, but the distribution of dE and dQ differ since $\rho \simeq P_e$ only at depth (where most of the cooling occurs) (Athay, 1972b).

Although not included in the cooling, the H9 (3835 Å) emission is calculated for the finished models with the same methods, for comparison with observations (Section 5.3). For this line, the two level approximation may not be as accurate. The net emission in the Balmer and Paschen continua is also determined for the models (Section 5.4). The He I line emission from the models is given by LaBonte (1978).

One other important contributor to cooling by hydrogen, especially at low temperatures, is H^- continuum emission (Brown, 1973). Using the form suggested by Osterbrock (1961) with the cross-section from Allen (1963),

$$dQ(H^-) = 4\sigma \; T^3(T-T_{min}) \; p_e \; (1-X) \; n_H \; 8\times10^{-26} \left(\frac{5000}{T}\right)^3 \qquad (12)$$

with σ the Stefan-Boltzmann constant, T_{min} the photospheric boundary temperature, p_e the electron pressure.

2.3.2 Metals

Metals cool the high temperature part of the flare. At the transition zone between the flare chromosphere and corona, the optical depth in all chromospheric transitions is clearly zero. The region just below this level has the lowest densities, highest temperatures and temperature gradients of the flare chromosphere, thus distributing its small total mass over several ionizations stages, and maintaining low optical depth. In contrast, the lower layers of the flare chromosphere with high densities, low temperatures and temperature gradients, have all their mass in the neutral atoms, whose lines are optically deep. A single correction factor applied to the optically thin emission must thus be $\simeq\rho$ at depth but $\simeq 1$ at the surface. P_e meets these requirements. Our relation for the metals cooling is

$$dQ(\text{metals}) = dE \; (\tau=0) \; P_e(\tau_{metals}) \qquad (13)$$

with the thin emission from Cox and Tucker (1969), approximately

$$dE(\tau=0) = 4.4 \times 10^{-36} \; T^{2.9} \; n_e^2 \; ; \quad T \lesssim 7.6 \times 10^4 K. \qquad (14)$$

The correction for optical depth is most important at low temperatures, and the value of τ_{metals} should apply to the species which contribute to the cooling at those temperatures; principally O I and C I. Since these atoms have first excitation and ionization potentials nearly equal those of hydrogen, we use

$$\tau_{metals} = A_{metals} \; \tau_{Lyman\ \alpha} \qquad (15)$$

with $A_{metals} = 10^{-3}$ the relative abundance by number.

Equations (13) and (15) represent the main effects of optical depth. One factor not allowed for is the increase in n_U above its optically thin value due to scattering, so the cooling by metals may be underestimated. This issue will be discussed in Section 4.2.2.

2.3.3 Explosion Level

Equation (14) is valid up to 76 000 K; from 76 000 to ≈260 000 K, dE is nearly constant, and above 260 000 K, decreases with temperature (Cox and Tucker, 1969). Thus for T≳300 000 K, the atmosphere is thermally unstable, and heats to coronal temperatures. With the cooling rate constant between 76 000 and 260 000 K, the lower temperature can be taken as the onset of instability, with no increase in cooling available to match increased heating. This is an

upper limit to the temperature of the part of the flare in radiative equilibrium. Higher parts of the atmosphere "explode" or free expand into the corona (Lin and Hudson, 1976).

By equating the maximum cooling rate with the electron heating, a value for the column density at the explosion level can be found, and thus $\mathcal{E}_x$, the lowest energy electron which participates in the radiatively stable flare. This in turn gives the total energy flux in the radiative flare,

$$F_{rad} = F_{20} \left(\frac{\mathcal{E}_x}{20} \right)^{1-\gamma} \qquad (16)$$

If the number density n is exponentially decreasing with height, as in an isothermal hydrostatic gas, and nearly so in the model atmosphere, then

$$F_{rad} \propto F_{20}^{\left(\frac{4}{\gamma+3}\right)} \; . \qquad (17)$$

While F_{20} changes by 10^3, F_{rad} changes by only ≈50 (for $\gamma=4$).

Because the cooling rate is constant between 76 000 and 260 000 K, the material is indifferent to exactly what its temperature is within that range. At the top of the radiatively stable flare, all temperatures between 1 and 3×10^5 K should be equally represented.

2.4 Solution Procedure

Equilibrium is assumed, so at each height the sum of radiative cooling losses due to HI, H^- and metals (L) must equal the sum of heating gains due to electrons and nonflare processes (G). With the total density fixed and the ionization determined simultaneously with the cooling, only the temperature distribution needs to be adjusted to obtain a solution.

An iterative scheme is used. The flare explosion level is found and an initial guess made at the temperature distribution using that point as a boundary condition. The heating and cooling for that distribution are computed, and the temperature distribution changed to make the ratio of heating to cooling closer to 1. The magnitude of the temperature correction at each step is found from the quantity $(G-L)(dL/dT)^{-1}$, with dL/dT the change in cooling rate per change in temperature between two successive temperature distributions. (Only the cooling is used because the heating is insensitive to temperature.) Each temperature distribution is smoothed to remove unphysical spikes or local inversions. Numerical tests show this procedure is convergent and stable. In the final models, the heating and cooling are equal within 5% at each point, on average.

3. MODEL RESULTS

This section presents the numerical results of the calculations. As we have noted, strict consistency of the results and the physical assumptions is not guaranteed in advance, because of the numerical nature of the computation. Questions of validity are discussed in Section 4.

3.1 Temperature

Figure 1a,b,c shows the temperature profiles for the γ=3, 4, 5 models, respectively. Curves are labeled by the value of $\log(F_{20})$. The initial quiet model is labeled Q.

Obviously, for larger F_{20} the heating of the chromosphere extends deeper. For example, in the γ=4 models, as F_{20} increases from 10^8 to 10^{11}, the explosion level moves inward from a density $\simeq 3\times10^{11}$ to $\simeq 3\times10^{12}$ cm^{-3}. The minimum electron energy penetrating to this level, ε_x, increases from 9 to 24 keV, and the total energy flux dumped into the radiative region below the explosion level increases from $\simeq 10^9$ ($F_{rad} \simeq 10\ F_{20}$) to $\simeq 5\times10^{10}$ ($F_{rad} \simeq \frac{1}{2}F_{20}$). Since the values of ε_x are within the observed range of the hard X-ray power law spectrum, no significant extrapolation of that spectrum to lower energies is needed to produce the radiative flare.

Another expected result is that the temperature gradient varies directly with γ. For a given value of F_{20}, a high γ

beam has a larger fraction of low energy electrons, which heat near the surface; a low γ beam has a larger fraction of high energy electrons, which heat at depth. Near 500 km, the γ=3 models have temperatures nearly those of γ=5 models with 100 times larger F_{20}. The more intense γ=3 beams appear capable of penetrating below the temperature into the photosphere; this is not in fact correct (Section 4.1).

The only notable structure to the temperature profiles is the appearance of a bump (temperature excess) near 1000 km and 15 000 K, in the models with large F_{20}. The bump, when present, is the region where the cooling changes from metals dominated to hydrogen dominated. Its size and presence depends strongly on the value of the metals cooling. The bump is a response of the models to the weak dependence of the hydrogen losses on F_{20} (Section 3.5).

3.2 Energy Balance

Figure 2a,b shows the energy balance for the central models of our grid (γ=4, $F_{20} = 10^9$, 10^{10}). These illustrate the features seen in all the models. Note that the 10^{10} model has a temperature bump, while the 10^9 does not.

As expected, metals cool the highest, hottest part of the flare, T$\geq$14 - 20 000 K over all models. Hydrogen lines cool the middle part, and H^- the lowest, coolest part. More interesting is the result that in the region cooled by hydrogen lines, Hα dominates. Lyα cooling peaks higher, in the region controlled by metals.

The thickness of the layer cooled by the hydrogen lines varies inversely with F_{20}. It is $\gtrsim$500 km at $F_{20} = 10^8$, but $\lesssim$100 km at $F_{20} = 10^{11}$. The difference is provided by the metals cooling extending to greater depth, and the rapid increase in H^- emission. In addition, Hα and Lyα are saturated, in the sense that their volume cooling dQ varies little, around 10 ergs $cm^{-3}s^{-1}$. The H^- and metals cooling show much larger ranges. This saturation produces the bump in the temperature profiles, as higher temperatures are needed to maintain the cooling at depth.

The total contribution of hydrogen to the flare cooling is small. The ratio of Q(metals)/Q(H) ranges from $\simeq$10 at $F_{20} = 10^8$ to $\simeq$30 at $F_{20} = 10^{11}$. Essentially all the energy output is in metals emission. This is a response to the exponential form of the energy input. Fully half of the total flux F_{rad} is dumped in the top 50 to 100 km of the radiative flare, where it is balanced by emission at temperatures of 50 to 76 000 K (up to 300 000 K).

3.3 Electron Density

Figure 3a,b,c shows the electron density distribution for the γ=3, 4, 5 models, respectively. In each case, total ionization extends down to some depth, below which the electron density drops off rapidly. The peak value of n_e

increases with F_{20}. At a given F_{20}, a high γ model has a lower peak n_e and a steeper drop off than a low γ model. The maximum values of n_e range from 3×10^{12} to $\simeq1\times10^{14}$ cm^{-3}, but have validity problems (Section 4.1).

3.4 Hydrogen Level 2 Density

Figure 4 shows the hydrogen level n=2 density distribution. The height of peak n=2 density coincides with that of the peak n_e. As such, it shares the validity problems of n_e.

The peak n_2 density is 1 to 300 km below the maximum Hα volume cooling, and 2 to 500 km below the Lyα maximum; the larger separations occur at larger F_{20}. Column integral values of n_2 range from 3×10^{14} to 3×10^{16} cm^{-2} (Hα optical depths $\simeq10^2$ to 10^4). Halfwidth of the n_2 density ranges from 75 to $\simeq$200 km, being thinner for larger F_{20}.

3.5 Self-Consistent Emission

Tabel 1 gives the H^-, Hα and Lyα emission (ergs $cm^{-2}s^{-1}$) for the models. As these radiations were computed self-consistently with the models, they should be accurate if the assumptions are valid.

Although necessary for the energy balance, the H^- emission is negligible. The contrast of the H^- continuum is $\lesssim$1% in the visible, even for the strongest models. Even this small emission is probably not present, however

(Section 4.1).

The line emission is concentrated near $\tau=1$, even though the cooling is deeper; the photons diffuse to the surface to escape. We only consider the total line emission because the line profiles for this type of static model are strongly self-reversed (Canfield, 1974a). However, macroscopic turbulent velocities only a factor of 2 to 3 larger than the model thermal velocities would smooth out the profiles into better agreement with observations. This extra broadening would alter the line optical depth scales, but not greatly affect the computed cooling; $\tau\propto v^{-1}$, while the line cooling is typically spread over a range of 100 in τ.

Hα emission only increases by a factor of 5 between the $F_{20} = 10^8$ and 10^{11} models, and is independent of γ. The Hα equivalent width ranges from 5 to 25 Å of the nearby continuum. The Lyα to Hα energy ratio varies from $\simeq$1 in the 10^8 models to $\simeq$2 in the 10^{11} models. Because neither Hα nor Lyα vary greatly among the models, they might also be insensitive to changes in the model physics; for example, order of magnitude changes in the metals cooling. This has been shown in numerical tests.

3.6 Other Emission

Table 2 gives the H9 (3835 Å), Balmer continuum, and Paschen continuum emissions, computed from the final models.

The calculations of these transitions were not included in the model cooling, as they were assumed to emit much less than Hα or Lyα.

H9, unlike Hα, varies greatly in response to F_{20}. The H9 emission increases by ≈400 as F_{20} goes from 10^8 to 10^{11}. There is also a strong γ dependence, with H9 emission 10 times larger at γ=3 than γ=5, at fixed F_{20}. The H9 emission is much less than Hα in the weak models, but nearly equal in the strong models. The optical depth ranges from 0.7 to 70 with F_{20}; since τ<1 in the weak models, the emission computed is possibly in error.

As with H9, the Balmer and Paschen continua emissions vary strongly with F_{20} and γ. In the weak models each continuum emits less than Hα, but in the strong models, emits much more; the Balmer continuum emission in the strongest models nearly equals the total energy flux F_{rad}. However, the recombination continua are emitted at the electron density maximum, and vary as n_e^2. They are thus very sensitive to the problems with the maximum electron density (Section 4.1).

The He I 584 Å, 10830 Å and 5876 Å (D_3) emission from a set of these models has been computed by LaBonte (1978). Those transitions do not affect the results described in this study. Like H9, the helium lines are very sensitive to F_{20}.

4. SELF-CONSISTENCY

In this section we test the model results for consistency with the initial assumptions.

4.1 Heating

At depth in the atmosphere, the energy flux deposited by the electron beam is too small to heat the atmosphere to the computed equilibrium state in the short duration of the flares. Brown (1973) assumed the equilibration time to be $t_T = nkt/G_F$, the time to heat the gas to the equilibrium temperature, but this is not correct in these models. A much stronger limit is the time required to ionize the gas, $t_I = n_e R_H/G_F$, R_H a Rydberg. Because the models are fully ionized to fairly low temperatures, $\approx 10^4$K, $n_e R_H > nkT$ from near the explosion level to below the electron density maximum. This constraint sets a stronger limit on the depth of flare heating than either the requirement of temperature equilibrium or the effect of a high energy cutoff in the electron beam spectrum.

For the models, t_I is largest at the electron density maximum, (n_e^{max}), and varies between 40 and 120 seconds. These times are much larger than the 10 s characteristic time of the events. However,

$$t_I \propto N^{-\left(\frac{\gamma+1}{2}\right)} \propto n^{-\left(\frac{\gamma+1}{2}\right)},$$

and the condition $t_I \lesssim 10$ s is achieved by moving to a density a factor of 2 or 3 lower than n_e^{max}, at about 100 km higher altitude. This suggests the flare models (temperature and density profiles) should be truncated at about 100 km above the computed n_e^{max}.

The effect on the emitted radiation of removing the lowest part of the models varies for the different transitions. Lyα and Hα will be only slightly affected since they are produced well above n_e^{max}. Even H9 may only be altered by a factor of 2 or 3. The continua are greatly changed. H^- is produced entirely below n_e^{max}, and would be effectively reduced to zero. The recombination continua, being proportional to n_e^2, would decrease by about an order of magnitude; this is an improvement from the standpoint of consistency, given the large computed values.

For all higher altitudes in the radiative flare, the energy input is sufficient to heat and ionize the chromosphere to the computed equilibrium. Above the explosion level, the product of heating and flare duration will set the temperature, with radiative cooling negligible.

4.2 Cooling

4.2.1 Atomic Equilibrium

For the radiative equilibrium to be actually achieved, the ionization fraction and level populations must

reach the equilibrium values in the flare duration. This requires all important atomic rates to be $>(10\ s)^{-1}$. In general the slowest rates, which control the equilibration time, are the first excitation rate, $C_{12} \propto n_e \exp(-h\nu/kT)$ (e.g., Lyα collisional excitation) and radiative recombination, $R_k \propto n_e\, z^2\, T^{-\frac{1}{2}}$.

For the hydrogen system, the time constraint is met by all models in the region of Hα and Lyα cooling. At depth both C_{12} and R_k are reduced below the limit by the decreasing electron density and temperature. In the weak models, R_k also fails at altitude, because of the decreasing density; a reduction in the neutral fraction, thus optical depth, is indicated at high temperature in the weak models. C_{12} remains above the limit at altitude as the temperature dependence outweighs the density decrease.

The metals (in all ionization stages) have C_{12} about equal to hydrogen, and should also meet the equilibrium condition. In addition, the charge dependence of R_k implies that the higher ionization stages, important to high temperature cooling, will also equilibrate.

4.2.2 Optical Depth Correction for Metals

The approximation used to correct for the optical depth of the metal lines can be tested by applying the same procedure to hydrogen and comparing with the properly

computed results. For this test we compare the peak value of the Lyα cooling, at T = 20 to 30 000 K, with the values predicted using first, the optically thin formula only, and second, the optically thin value corrected by P_e(Lyα). Subordinate lines contribute little to the hydrogen cooling at this temperature.

The result of this test is that our corrected form is better than the uncorrected optically thin form. The optically thin case predicts emission which is 25 to 200 times larger than the exact result; the error increases with F_{20}. The corrected form predicts emission 5 to 40 times smaller than the exact result; the error decreases with increasing F_{20}. The worst corrected case is nearly as good as the best thin case. However, while the corrected form is a useful order of magnitude estimator, it is clear that a more exact calculation of the metals must be done in any improved model.

4.2.3 Balmer Decrement

In computing the models it was assumed that the cooling due to atomic hydrogen was dominated by the leading lines Lyα and Hα. In the weak models this is a good approximation, but the subsequent calculation of the H9 line and the recombination continua shows this is incorrect in the strong models. (Brown's [1973] models were similar to our weak models, therefore Canfield [1974a] found Hα and Lyα dominant.)

Even allowing for the reduction in emission suggested in Section 4.2.1, the continua contribute more than the lines. Further, the H9 values suggest a small Balmer decrement, with many lines comparable in intensity to Hα. (The H9 calculation may itself be incorrect, if the two level approximation fails; the upper level can decay through other transitions with lower optical depth, and is more closely coupled to the continuum than the lower levels.) In the strong models, the hydrogen cooling may be underestimated by an order of magnitude. More cooling would give lower temperatures and ionization than the computed models.

The onset of much higher cooling at large energy fluxes would in effect produce a saturation of the atmosphere. Beyond some critical energy flux, perhaps $F_{20} \geq 10^{10}$, only small increases in temperature and ionization would be needed to greatly increase the cooling and balance the flare heating. The already weak dependence of the Hα and Lyα emission on F_{20} would be further reduced, while the higher excitation lines would be very sensitive to large values of F_{20}.

4.3 Atmospheric Stability

The chromospheric density distribution was assumed not to relax to a new hydrostatic form consistent with the flare temperatures in the flare duration. In the models this is true. The absolute value of the pressure gradient

$\lesssim$3 times the preflare hydrostatic gradient. Mass accelerations are thus $\lesssim$3 times gravity, with velocities and displacements negligible in 10 s ($\lesssim$8 km s^{-1}, $\lesssim$14 km).

A more serious problem occurs at the flare explosion level. The temperature of the gas just above that point increases continually, because the electron heating exceeds the radiative cooling. In 10 s, temperatures of 1 to 4×10^7K are reached ($dT \simeq dt\ G_F/2nk$). With the density continuous through this level but the temperature discontinuous, a pressure jump of order 100 is formed, generating a shock wave. Of course, the shock actually forms in a few seconds, with an initially lower amplitude.

An instability at this level is unavoidable, because the heating is independent of temperature while the radiative cooling is a decreasing function of temperature. For hydrostatic equilibrium the 10^7K material should be 100 times less dense than the 10^5K gas, but for radiative balance against the heating, the 10^7K gas must be $\simeq$10 times more dense than the 10^5K gas (Cox and Tucker, 1969). These conditions cannot be met simultaneously. Once the temperature rises above 10^5K, further heating is unchecked, leading to pressure instability. The instability is not resolved in a finite time, and gas motions must continue as long as the electron heating. The idea that a long-lived electron heated flare can be considered relaxed (Brown, 1973) is

wrong; indeed, the hydrodynamic effects should be larger, having time to fully develop. Other types of long-lived flare heating which are temperature sensitive, for example conduction, apparently do permit static solutions (Moore and Fung, 1972; Shmeleva and Syrovatskii, 1973).

The shock moving into the chromosphere is compressive, with the density behind $\gtrsim$4 times the ambient. Once the density of the 10^7K gas is 10 times its initial value, radiation can balance the heating. Therefore, when the shock penetrates only a factor $\lesssim$2.5 in density, about 200 km, the heating is balanced and the temperature stabilized. Further penetration (density increase) would lower the temperature, and since the cooling coefficient at all temperatures from $10^4<T<10^7$K is larger than that at 10^7K, the gas would cool catastrophically toward the lower temperature, with a time scale of a few seconds. Some residual of the shock would certainly continue deeper, in the form of bulk motions, turbulence, or perhaps heating. An interesting alternative model to ours would be one in which the chromosphere is not heated directly by the electron beam, but indirectly by the shocks it produces; the large energy fluxes dumped at the top being convected downward in shocks.

One further problem is that the rate of temperature increase varies as $N^{-\left(\frac{\gamma+1}{2}\right)}$,

thus rapidly increasing with height as long as the power law electron spectrum continues to lower energies. These hotter layers will dump more energy into gas motions. The extent of the chromospheric disruption will thus depend on the low energy electron spectrum. Until direct measurements are made, this will remain a fundamental uncertainty in the models.

5. COMPARISON WITH OBSERVATIONS

Although the models are inconsistent at the top and bottom, in the middle layers where the hydrogen line emission is produced they may be valid. It is of interest to compare the model predictions with observations as a further test of validity. One problem is the limited data on rapid flashes, or even the normal flash phase of flares; comparison in some cases may not be appropriate. Generally, data are available only for large flares, therefore certain properties cannot be accurately tested, for example, the weak dependence of Hα and Lyα emission on F_{20}.

5.1 Lyα to Hα Ratio

The Lyα to Hα energy ratio is predicted to be 1 to 2. Zirin (1978) has pointed out that this ratio is of order 1 in flares, although the data are sparse. Because this ratio

varies so little in the models, it is conceivable that it can be shown analytically to reduce to a combination of atomic constants; we have not been able to do so.

5.2 Hα

The Hα equivalent widths predicted, 5 to 25 Å are too large by a factor of 2 or 3. The largest observed flash phase equivalent widths are 10 to 15 Å (Svestka, 1976). In small events, widths or order 1 or 2 Å are indicated (Zirin, 1977). The Hα optical depths (and integral values of n_2) are in the range of observed flares, but will be reduced by the various model problems by a factor of 2 or 3.

5.3 H9

The predicted H9 emission may also be too large. The H9 emission in the August 4, 1972 1840 UT and 2140 UT events was $\simeq 6 \times 10^7$ and $1 - 2 \times 10^7$ ergs $cm^{-2} s^{-1}$ respectively (Zirin and Tanaka, 1973); the emitting areas $\simeq 2 \times 10^{17}$ and 5×10^{17} cm^2. The observed X-ray emission, converted to thick target electrons, implied $E_{20} = 5.4 \times 10^{28}$ and 1.4×10^{28} ergs s^{-1}, with $\gamma = 2.8$ and 2.5 (Lin and Hudson, 1976). If the electron flux is assumed to be confined to the H9 emission area, then $F_{20} = 2.7 \times 10^{11}$ and 2.8×10^{10} ergs $cm^{-2} s^{-1}$ are required. Using the $\gamma = 3$ models, the predicted H9 emission is 3×10^8 and 1×10^8 ergs $cm^{-2} s^{-1}$, much larger than observed.

However, it is clear that some of the nonthermal flux must be heating the much larger total flare area. For example, the Hα kernel alone has an area 25 times that of the H9 flashes in the 1840 UT flare. Given the high sensitivity of H9 to F_{20}, an alternate assumption could be made, that nearly all the nonthermal electrons are dumped outside the H9 area. The H9 area would then have F_{20} enhanced by only a factor of perhaps 3 above the flare average, rather than orders of magnitude. This would bring the predicted emission down closer to the observed values.

5.4 Continuum

The continuum emissions are strongly affected by the disequilibrium in the lower part of the models. (Note that with the factor of 2 or 3 reduction needed to correct this problem, the maximum electron densities in the models are in the observed range; Svestka [1976]). Considering this problem, the H^- continuum should be absent, and the hydrogen recombination continua emissions $\lesssim 0.1$ the values in Table 2. The recombination continua are emitted at a temperature of 15 000 K. The Paschen continuum should be nearly flat, with only ≈15% decrease in energy flux per Å between the Paschen and Balmer limits, and the Balmer jump about a factor of 16 in the same units.

The continuum emission in the August 7, 1972 1520 UT flare had two components: a group of knots, and a wave

(Machado and Rust, 1974; Rust and Hegwer, 1975). In the knots, emission at 4950 Å was $3 - 6 \times 10^6$ ergs cm^{-2} s^{-1} $Å^{-1}$, and a factor of 2 to 4 less at 5900 Å (brighter knots were bluer). In the wave, emission was 1.5×10^6 ergs cm^{-2} s^{-1} $Å^{-1}$ at 4950 and 5900 Å; between 4300 and 3700 Å there was a factor of 2 increase in intensity; and a Balmer jump of $\lesssim 2.5 \times 10^6$ ergs cm^{-2} s^{-1} $Å^{-1}$ was possible but not positively indicated. Areas were 6×10^{17} and 2×10^{17} cm^2. If all the X-rays were thick target and all the nonthermal electrons dumped in the continuum emission areas, then $F_{20} = 3.7 \times 10^{11}$ and 1.1×10^{11} ergs cm^{-2} s^{-1}, with $\gamma = 2.3$ (Lin and Hudson, 1976). Using the $\gamma=3$ models, Paschen emission of $\lesssim 5 \times 10^5$ and $\lesssim 1.6 \times 10^5$ ergs $cm^{-2} s^{-1} Å^{-1}$ is predicted. The Balmer jump in the wave would be $\lesssim 2 \times 10^6$ ergs $cm^{-2} s^{-1} Å^{-1}$.

These results show that most or all of the observed continuum must be produced by some process other than hydrogen recombination. The predicted recombination spectrum is too faint and red. The knots are even bluer than an H^- continuum, which would have the additional problem of being unable to rapidly vary in intensity (Rust and Hegwer, 1975), due to the long time needed to heat the layers emitting H^-.

5.5 Metals

All the models predict that the ratio of metals

emission at $\simeq 10^5$ K to hydrogen emission is 10, even (or, especially) considering hydrodynamic disruption. Many of the important lines at 10^5 K are in the wavelength range 300 to 1400 Å (Moore, 1976), so a comparison of Lyα to the other lines in this region should give a rough measure of the metals to hydrogen ratio. Older data on large flares (Hall and Hinteregger, 1969; Donnelly and Hall, 1973), with low time resolution and no spatial resolution, showed this ratio to be ≃1, with Lyα about equal to the sum of the metals emission. However, the data presented by Emslie and Noyes (1978) show that in small (5"), rapid (lifetimes 20 - 60 s) flash flares, several metal lines each equal to Lyα emission (see also Noyes et al., 1975). Thus the ratio of metals to hydrogen is ≳4, and considering the other metal lines not measured, the ratio could be ≳10, as predicted.

6. SUMMARY

We have attempted to model flares with rapid intensity fluctuation. The model balances nonthermal electron heating with thermal radiative cooling in a hydrostatic chromosphere.

The computed models show the initial assumptions are not correct throughout. The actual flare chromosphere cannot be static at high altitude (insufficient cooling) and does not reach thermal equilibrium at depth (insufficient heating). The middle layers, approximately where the

hydrogen emission is produced, may be valid, though. The timings and emissions in the middle layers are close enough to the required values that an equilibrium region cannot be ruled out, given the model simplicity.

A time dependent calculation is needed to prove the existence and extent of an equilibrium layer. Both the atmospheric structure and atomic equilibrium (ionization and excitation) must be time-variable. This calculation would also indicate whether the chromospheric heating is actually provided directly by the electron beam as assumed, or by the downward mixing of hot material by shocks.

Model-insensitive parameters such as the Lyα/Hα and metals/hydrogen emission ratios are correctly predicted. The Balmer lines Hα and H9 are brighter than observed; they would be reduced in a more exact model to give better agreement. Nonthermal line emission appears unnecessary in this type of flare. The predicted continuum emission is less than the observed, and the difference in spectral shapes suggests other emission processes produce the observed continuum.

In any improved model the radiative cooling should be computed more accurately. The assumption that Lyα and Hα dominate the hydrogen cooling is true only in weak models; other lines and continua contribute in the strong models. The metals emission for each species should be computed by the same technique used for hydrogen, rather than using

approximate forms.

The necessary improvements in the model will introduce great complexity. A more productive next step therefore may be to improve the observational data on rapid flash flares, which is currently quite limited. Such rapid flares are reasonably frequent; of 50 He I D_3 events observed at Big Bear Solar Observatory in 1974 and 1975, 3 showed emission areas evolving in times $\lesssim$10 s. A serious observing program would set exact standards for future models. Some questions would remain unanswered; spatially resolved hard X-ray spectra are needed to determine the actual intensity and distribution of thick target electrons in flares.

We thank R. Moore for useful discussions, and R. Canfield for other discussions on radiative cooling.

This research was supported by NASA under grant NASA NGR 05 002 034 and NSF under grant ATM76-21132.

REFERENCES

Allen, C.W.: 1963, Astrophysical Quantities, Athlone Press, London.

Athay, R.G.: 1972a, Ap.J. 176, 659.

Athay, R.G.: 1972b, Radiation Transport in Spectral Lines, Reidel Publishing Co., Dordrecht, Holland.

Beckers, J.M.: 1972, Ann. Rev. Ay. Ap., 10, 73.

Bessey, R.J. and Kuperus, M.: 1970, Solar Phys. 12, 216.

Brown, J.C.: 1973, Solar Phys. 31, 143.

Canfield, R.C.: 1974a, Solar Phys., 34, 339.

Canfield, R.C.: 1974b, Ap.J. 194, 483.

Canfield, R.C.: 1974c, AFCRL-TR-74-0158, Env. Res. Paper No. 47.

Cox, D.P. and Tucker, W.H.: 1969, Ap.J. 157, 1157.

Datlowe, D.W.: 1974, in Solar γ-, X- and EUV Radiation, S.R. Kane (ed.), IAU Symp. 68, Reidel Publishing Co., Dordrecht, Holland.

Donnelly, R.F.: 1971, Solar Phys., 20, 188.

Donnelly, R.F., and Hall, L.A.: 1973, Solar Phys. 31, 411.

Emslie, A.G. and Noyes, R.W.: 1978, Center for Astrophys. preprint 897.

Frost, K.J. and Dennis, B.R.: 1971, Ap.J., 165, 655.

Hall, L.A. and Hinteregger, H.E.: 1969, in Solar Flares and Space Research, C. de Jager and Z. Svestka (eds.), COSPAR 11, 81, Reidel Publishing Co., Dordrecht, Holland.

Heasley, J.N., Mihalas, D. and Poland, A.I.: 1974, Ap. J. 192, 181.

Heyvaerts, J., Priest, E.R. and Rust, D.M.: 1977, Ap.J. 216, 123.

Hudson, H.S.: 1972, Solar Phys. 24, 414.

Kahler, S.W.: 1977, Ap.J. 214, 891.

Kahler, S.W. and Kreplin, R.W.: 1971, Ap.J. 168, 531.

Kane, S.R. and Anderson, K.A.: 1970, Ap.J. 162, 1003.

Knight, J. and Sturrock, P.A.: 1977, Ap.J. 218, 306.

Kulander, J.L.: 1976, Solar Phys. 48, 287.

LaBonte, B.J.: 1978, Big Bear Solar Obs. Preprint #0170.

Lin, R.P. and Hudson, H.S.: 1976, Solar Phys. 50, 153.

Machado, M.E. and Rust, D.M.: 1974, Solar Phys. 38, 499.

Moore, R.L.: 1976, Big Bear Solar Obs. Preprint #0158.

Moore, R.L. and Fung, P.C.W.: 1972, Solar Phys. 23, 78.

Noyes, R.W., Foukal, P.V., Huber, M.C.E., Reeves, E.M., Schmahl, E.J., Timothy, J.G., Vernazza, J.E. and Withbroe, G.L.: 1975, in Solar γ-, X- and EUV Radiation, S.R. Kane (ed.), IAU Symp. 68, Reidel Publishing Co., Dordrecht, Holland.

Osterbrock, D.E.: 1961, Ap.J. 134, 437.

Peterson, L.E., Datlowe, D.W. and McKenzie, D.L.: 1973 in High Energy Phenomena on the Sun, R. Ramaty and R.C. Stone (eds.), NASA SP342, 132.

Rust, D.M. and Hegwer, F.: 1975, Solar Phys. 40, 141.

Sheeley, N.R., Bohlin, J.D., Brueckner, G.E., Purcell, J.D., Scherrer, V.E., Tousey, R., Smith J.B., Speich, D.M., Tandberg-Hanssen, E., Wilson, R.M., DeLoach, A.C., Hoover, R.B., and McGuire, J.P.: 1975, Solar Phys. 45, 377.

Shmeleva, O.P. and Syrovatskii, S.I.: 1973, Solar Phys. 33, 341.

Sturrock, P.A.: 1968, in Structure and Development of Solar Active Regions, K.O. Kiepenheuer (ed.), IAU Symp. 35, 471, Reidel Publishing Co., Dordrecht, Holland.

Svestka, Z.: 1976, Solar Flares, Reidel Publishing Co., Dordrecht, Holland.

Syrovatskii, S.I. and Shmeleva, O.P.: 1972, Sov.A.J. 16, 273.

Van Beek, H.F., Hoyng, P. and Stevens, G.A.: 1973, in Collected Data Reports on August 1972 Solar Terrestrial Events, World Data Center A, Report UAG 28, Part II, 319.

Vernazza, J.E., Avrett, E.H. and Loeser, R.: 1973, Ap.J. 184, 605.

Vorpahl, J.A.: 1972, Solar Phys. 26, 397.

Zirin, H.: 1973, Vistas in Astron. 16, 1.

Zirin, H.: 1977, Big Bear Solar Obs. Preprint # 0165.

Zirin, H.: 1978, Big Bear Solar Obs. Preprint # 0172.

Zirin, H. and Tanaka, K.: 1973, Solar Phys. 32, 173.

Table 1

EMISSIONS INCLUDED IN COOLING

	Lyα			Hα			H^-		
F_{20}	γ = 3	4	5	3	4	5	3	4	5
10^8	4.4_7	5.1_7	5.6_7	4.5_7	4.4_7	4.2_7	3.4_6	1.7_6	1.2_6
10^9	1.3_8	1.3_8	1.2_8	1.1_8	9.8_7	8.7_7	2.5_7	8.2_6	4.2_6
10^{10}	2.9_8	2.6_8	2.4_8	1.8_8	1.6_8	1.4_8	1.7_8	4.5_7	1.8_7
10^{11}	6.3_8	4.9_8	4.0_8	2.7_8	2.3_8	2.1_8	7.9_8	2.1_8	7.9_7

All quantities are in ergs cm^{-2} s^{-1}.

$2_8 \equiv 2 \times 10^8$.

Table 2

EMISSIONS COMPUTED FROM FINAL MODELS

	H9			Paschen Continuum			Balmer Continuum		
F_{20}	γ = 3	4	5	3	4	5	3	4	5
10^8	2.8_5	2.4_5	2.0_5	9_6	6_6	4_6	3_7	2_7	1.4_7
10^9	3.9_6	1.0_6	6.3_5	2_8	6_7	3_7	7_8	2_8	1_8
10^{10}	7.2_7	1.2_7	4.2_6	2_9	6_8	2.4_8	6_9	2_9	8_8
10^{11}	2.0_8	9.6_7	2.5_7	9_9	6_9	9_8	3_{10}	2_{10}	3_9

All quantities are in ergs cm^{-2} s^{-1}.

$2_8 \equiv 2 \times 10^8$.

FIGURE CAPTIONS

Figure 1

Temperature profiles of the flare models. The initial quiet chromosphere is labeled Q. The flares are labeled with $\log(F_{20})$, F_{20} the energy flux in non-thermal electrons >20 keV. Height is measured from $\tau_{5000\ \mathring{A}} = 1$ in the continuum. Parts a, b, c of the figure give the models for γ=3, 4, 5 respectively, with γ the power law index of the hard X-ray spectrum emitted by the flare.

Figure 2

Energy balance for representative flare models. The energy input (ergs $cm^{-3}s^{-1}$) by the nonthermal electrons is balanced at each point by the thermal radiation cooling by metals, H^- continuum, and the Hα and Lyα lines of hydrogen.

(a) $F_{20}=10^9$ ergs $cm^{-3}s^{-1}$, γ=4

(b) $F_{20}=10^{10}$ ergs $cm^{-3}s^{-1}$, γ=4.

Figure 3

Electron density profiles of the flare models. Curves are labeled as in Figure 1. The flares are totally ionized above the electron density maximum. Parts a, b, c are for γ=3, 4, 5 respectively.

Figure 4

Hydrogen level n=2 density profiles of the flare models. Curves are labeled as in Figure 1. The n_2 maxima coincide with those of n_e. Parts a, b, c are for γ=3, 4, 5 respectively.

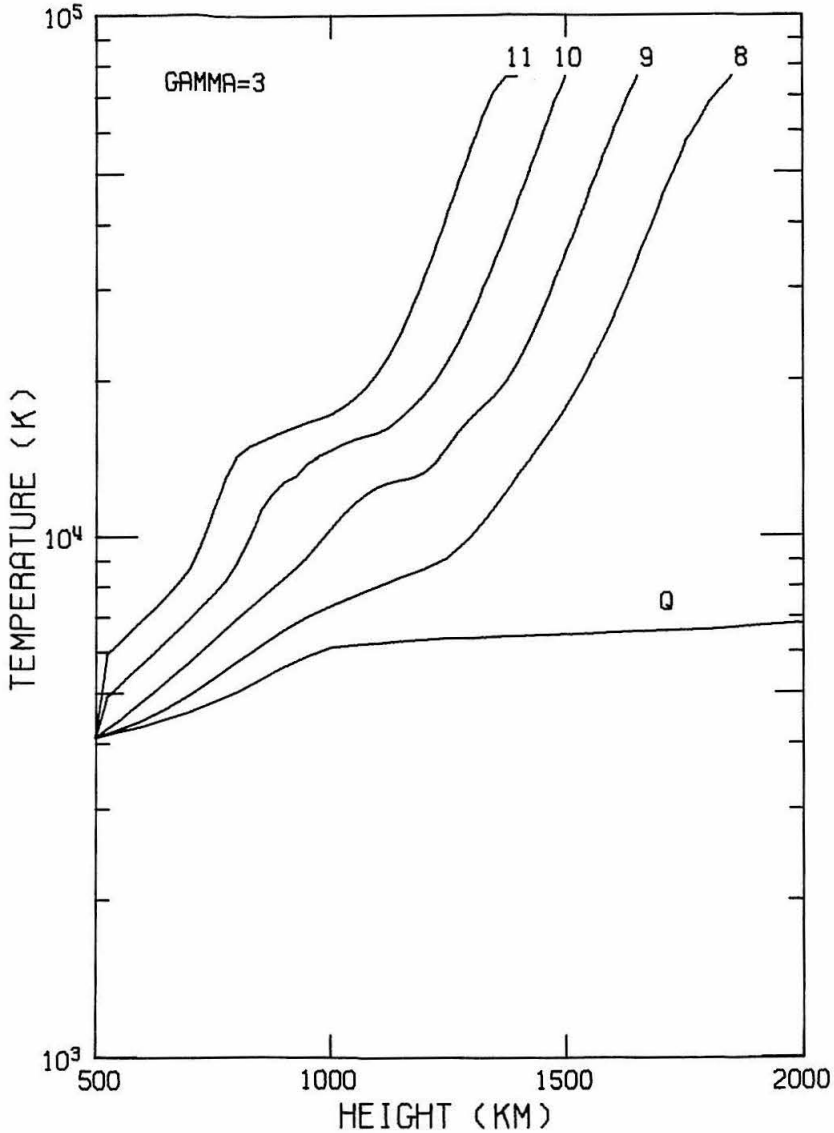

Figure 1a

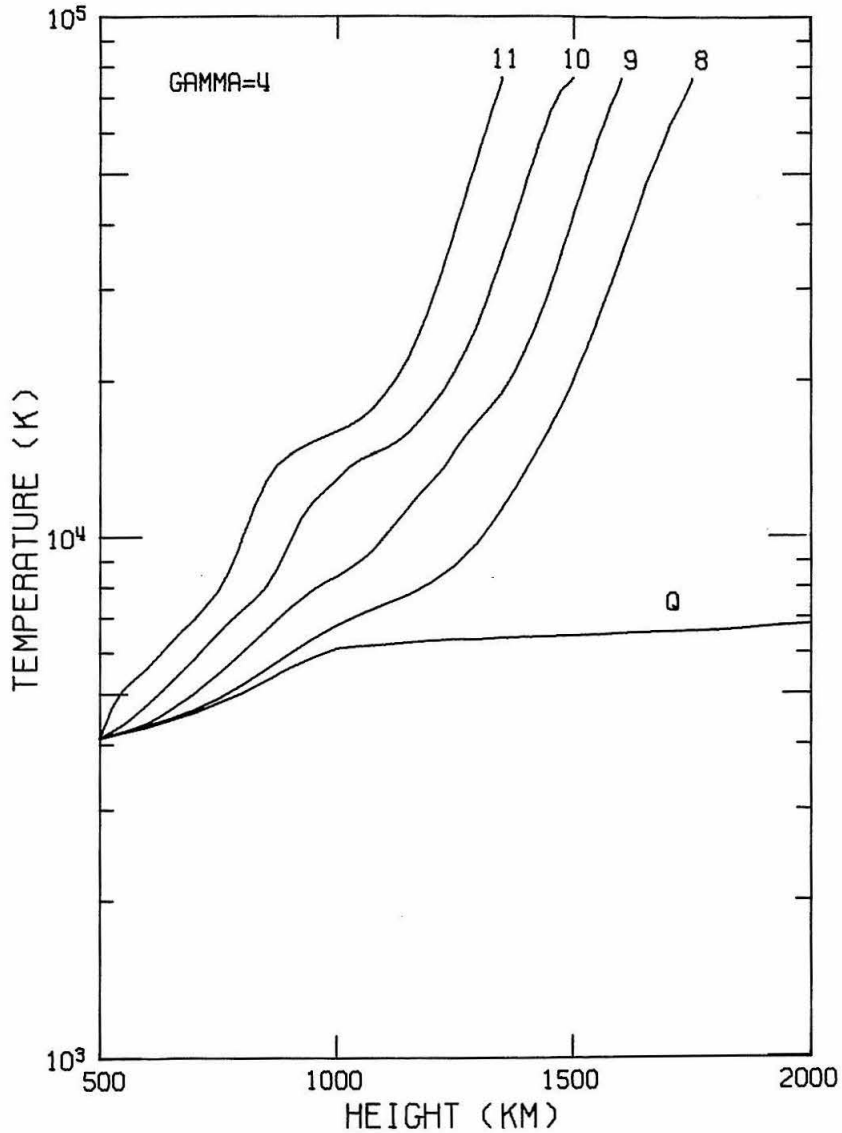

Figure 1b

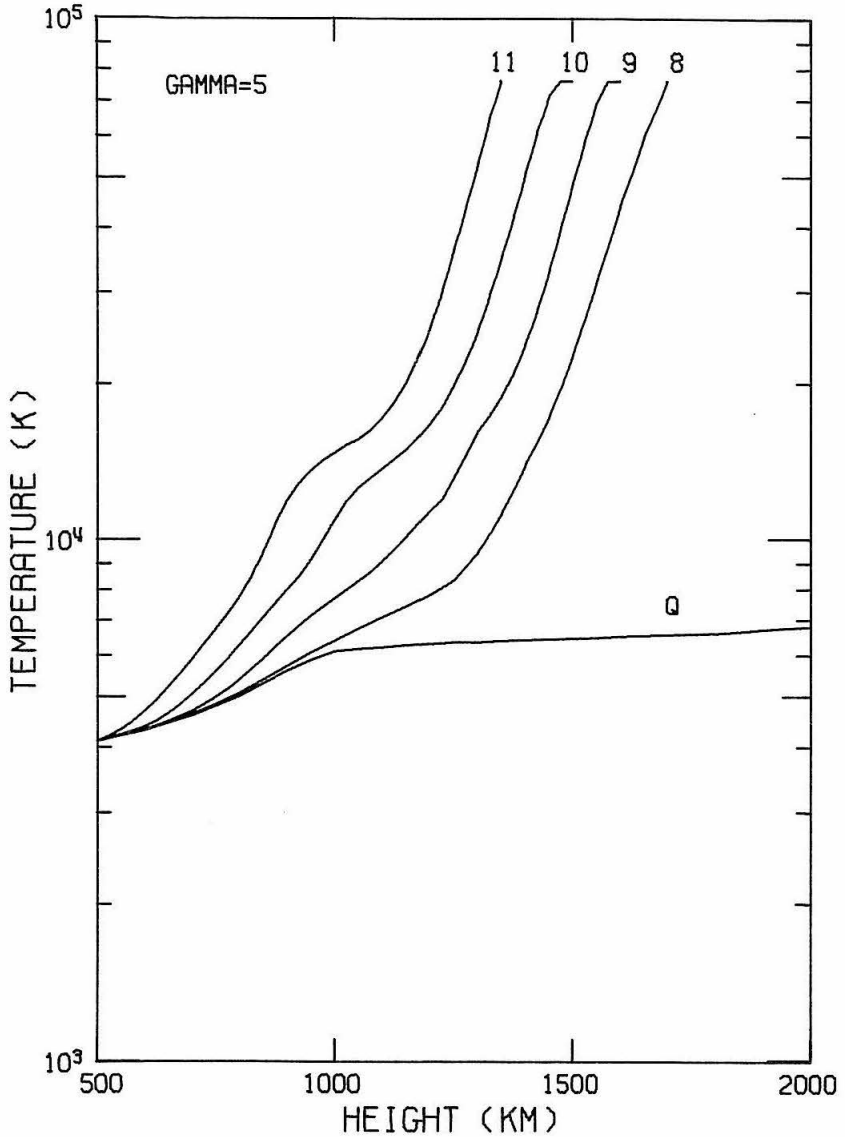

Figure 1c

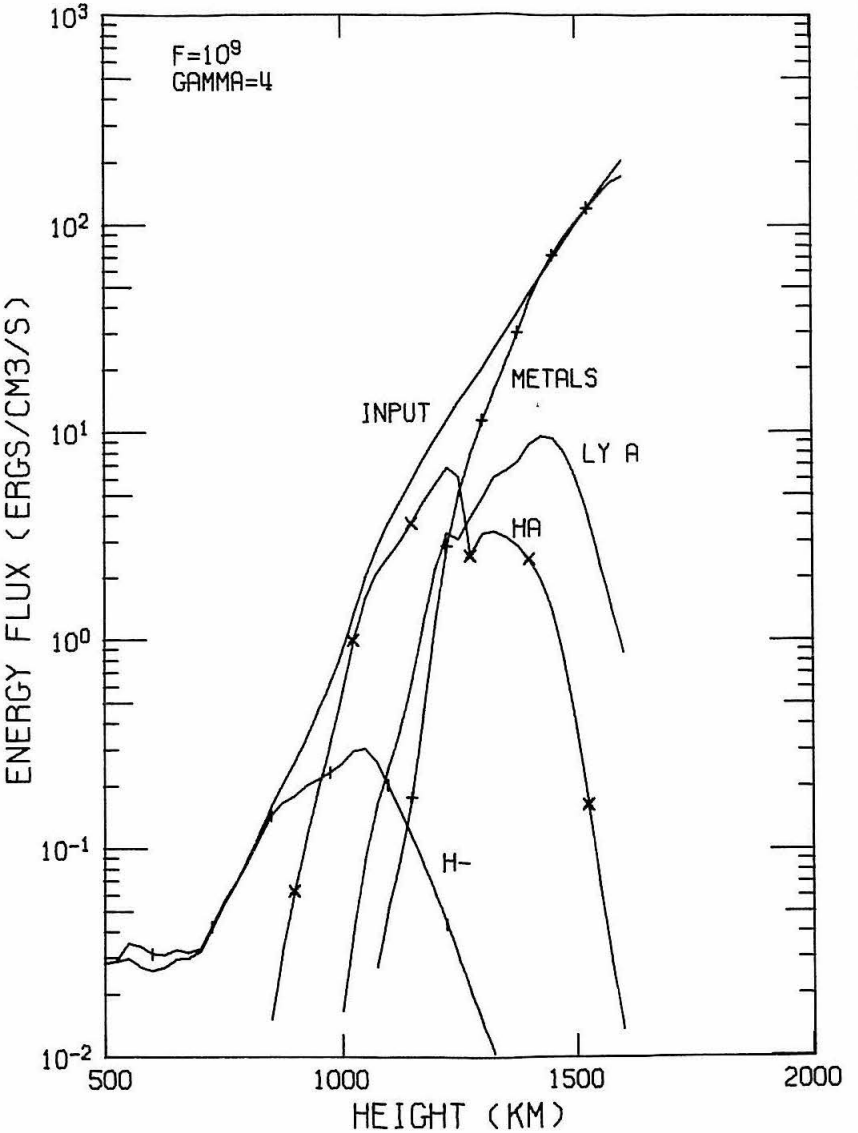

Figure 2a

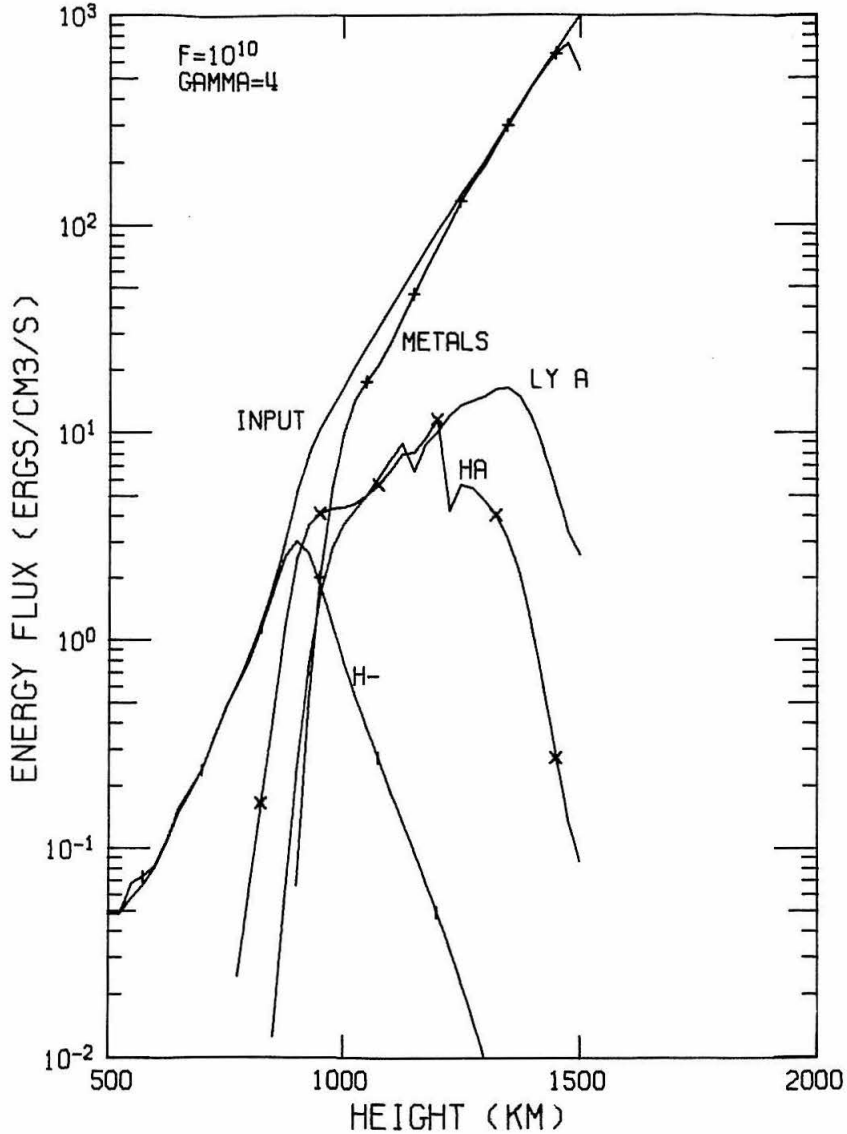

Figure 2b

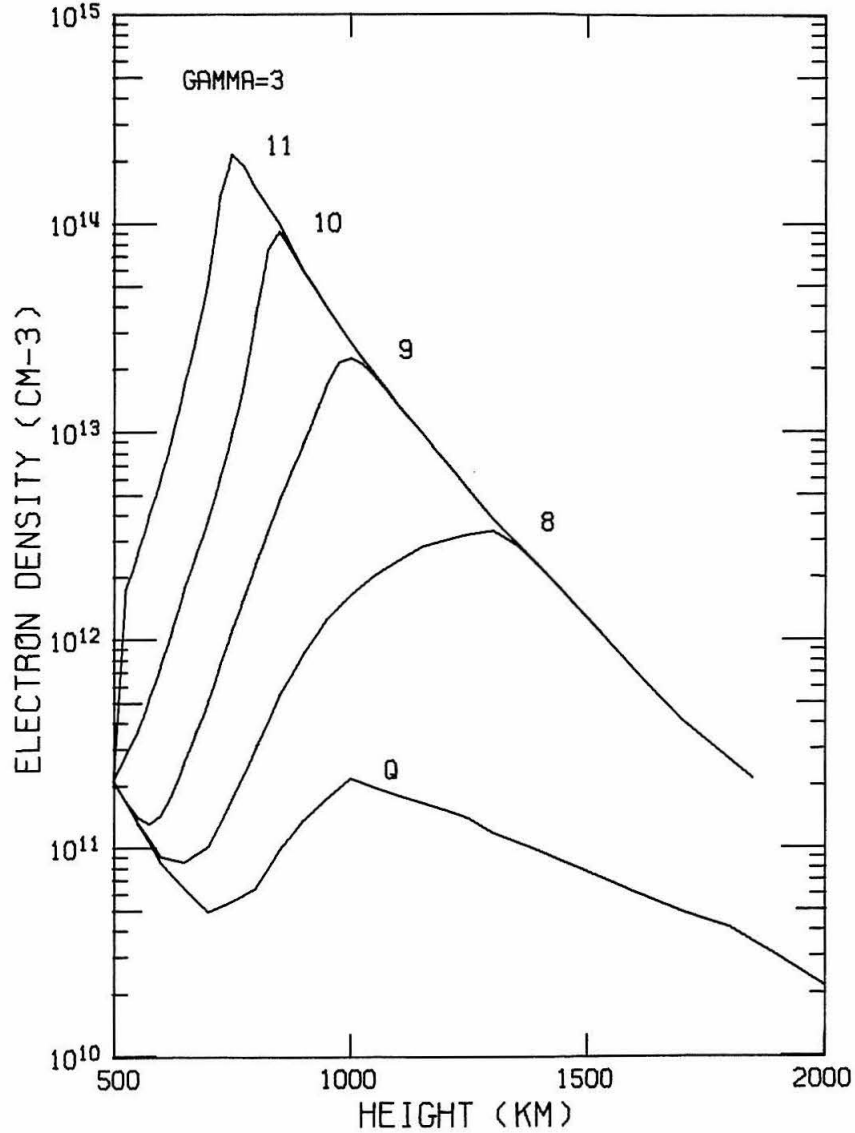

Figure 3a

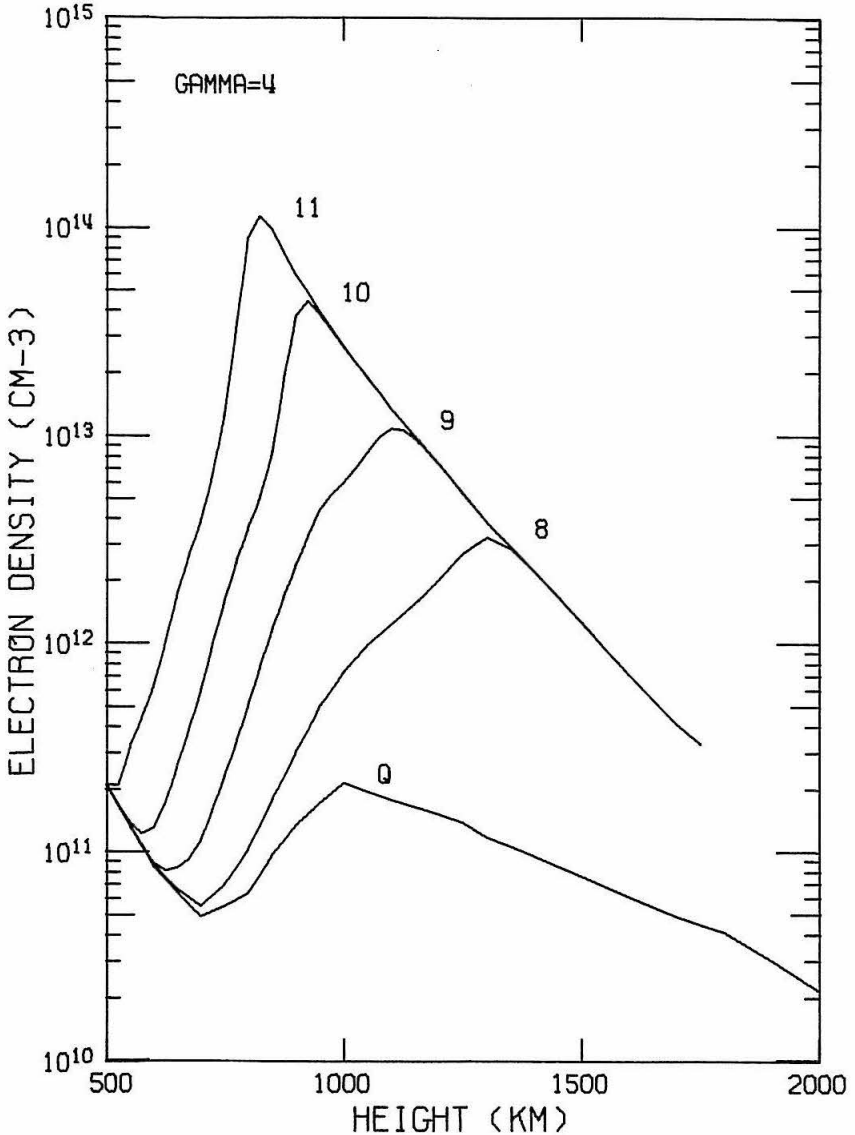

Figure 3b

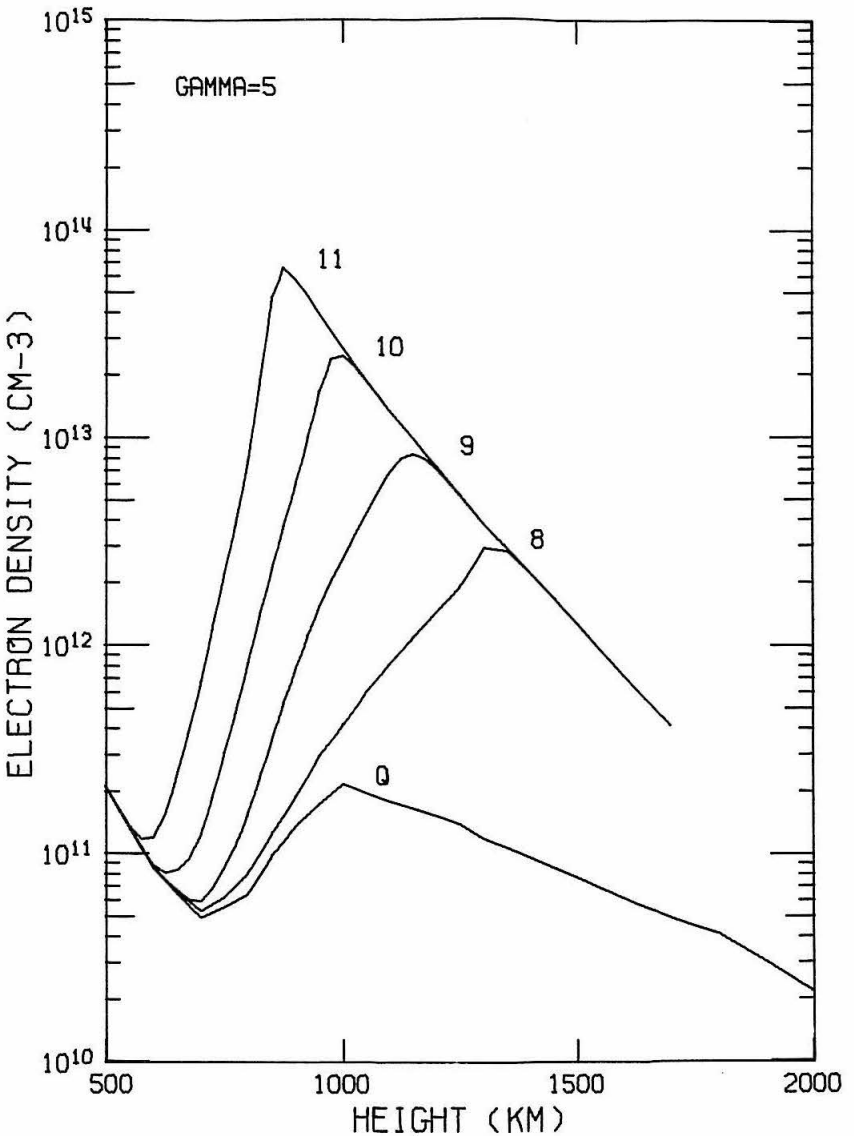

Figure 3c

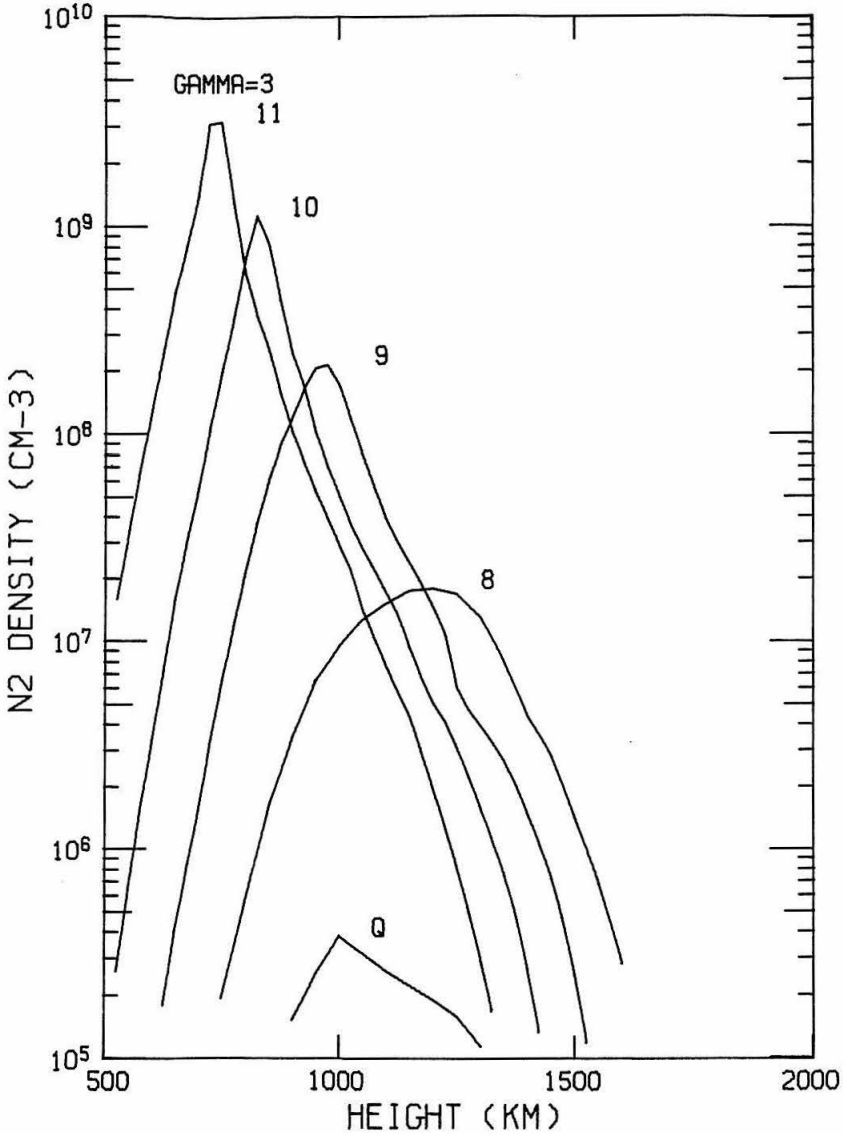

Figure 4a

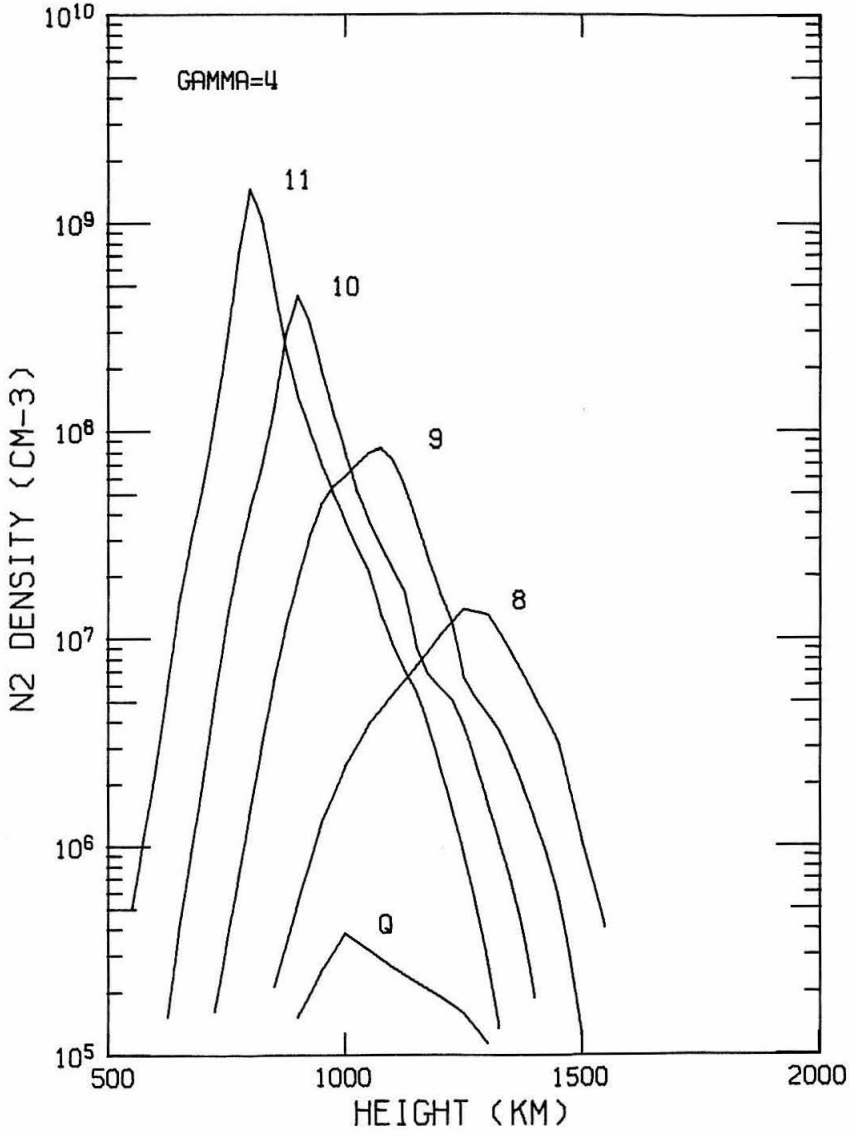

Figure 4b

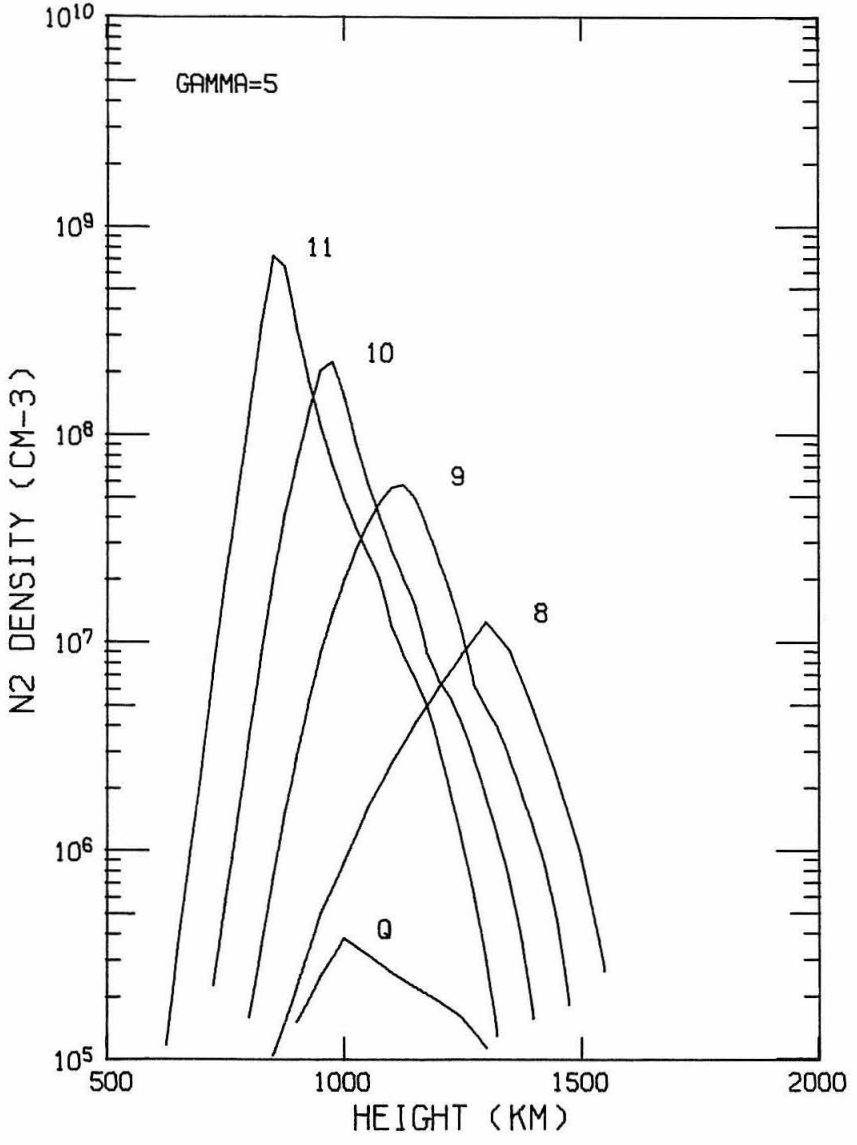
GAMMA=5
11
10
9
8
Q
N2 DENSITY (CM-3)
HEIGHT (KM)
10^{10}
10^{9}
10^{8}
10^{7}
10^{6}
10^{5}
500
1000
1500
2000

Figure 4c